

Observation of room-temperature magnetic skyrmions and their current-driven dynamics in ultrathin metallic ferromagnets

Seonghoon Woo¹, Kai Litzius^{2,3}, Benjamin Krüger², Mi-Young Im^{4,5}, Lucas Caretta¹, Kornel Richter², Maxwell Mann¹, Andrea Krone², Robert M. Reeve², Markus Weigand⁶, Parnika Agrawal¹, Ivan Lemesh¹, Mohamad-Assaad Mawass^{2,6}, Peter Fischer^{7,8}, Mathias Kläui^{2,3*} and Geoffrey S. D. Beach^{1*}

Magnetic skyrmions^{1,2} are topologically protected spin textures that exhibit fascinating physical behaviours^{1–6} and large potential in highly energy-efficient spintronic device applications^{7–13}. The main obstacles so far are that skyrmions have been observed in only a few exotic materials and at low temperatures^{1–4,6–8}, and fast current-driven motion of individual skyrmions has not yet been achieved. Here, we report the observation of stable magnetic skyrmions at room temperature in ultrathin transition metal ferromagnets with magnetic transmission soft X-ray microscopy. We demonstrate the ability to generate stable skyrmion lattices and drive trains of individual skyrmions by short current pulses along a magnetic racetrack at speeds exceeding 100 m s^{−1} as required for applications. Our findings provide experimental evidence of recent predictions^{10–13} and open the door to room-temperature skyrmion spintronics in robust thin-film heterostructures.

Whereas the exchange interaction in common magnetic materials leads to collinear alignment of lattice spins, in materials with broken inversion symmetry and strong spin–orbit coupling, the Dzyaloshinskii–Moriya interaction^{14,15} (DMI) can stabilize helical magnetic order^{1,2,4–6,16,17}. Of particular interest in such materials are magnetic skyrmions^{1,2}, particle-like chiral spin textures that are topologically protected from being continuously ‘unwound’. Magnetic skyrmions can arrange spontaneously into lattices^{1–6}, and charge currents can displace them at remarkably low current densities^{7–13}. However, experimental observation of these intriguing and useful behaviours at room temperature has so far remained elusive.

Skyrmion lattices were first observed in B20 compounds such as MnSi (refs 2,4), FeCoSi (ref. 3) and FeGe (ref. 5), whose non-centrosymmetric crystal structure gives rise to bulk DMI. Unfortunately, these materials order far below room temperature and only a few such compounds are known. DMI can also emerge at interfaces owing to broken mirror symmetry¹⁸. Spin cycloids and nanoscale skyrmion lattices have been observed in epitaxial ultrathin transition metal films by spin-polarized scanning tunnelling microscopy at ultralow temperatures^{6,17}. More recently, strong interfacial DMI in polycrystalline thin-film stacks

such as Pt/CoFe/MgO, Pt/Co/Ni/Co/TaN and Pt/Co/AlO_x has been inferred from field-induced asymmetries in domain wall motion^{19,20} and nucleation²¹. Micromagnetic simulations based on experimental estimates of DMI suggest that skyrmions can be nucleated, stabilized and manipulated by charge currents in such materials¹³, which could open the door to room-temperature skyrmion spintronics in robust thin-film heterostructures¹¹.

Here, we present direct observation of stable magnetic skyrmions and their current-driven motion in thin transition metal ferromagnets at room temperature. [Pt(3 nm)/Co(0.9 nm)/Ta(4 nm)]₁₅ and [Pt(4.5 nm)/CoFeB(0.7 nm)/MgO(1.4 nm)]₁₅ multilayer stacks (hereafter Pt/Co/Ta and Pt/CoFeB/MgO, respectively) with perpendicular magnetic anisotropy were studied with high-resolution magnetic transmission soft X-ray microscopy (MTXM, Fig. 1a). Pt in contact with Co is known to generate strong DMI (refs 20,22), whereas Ta and MgO generate very weak DMI (refs 22–24), so that a large net DMI is anticipated in these asymmetric stack structures.

Figure 1b shows full-field MTXM images of the domain structure in a Pt/Co/Ta film, which allow the DMI strength to be quantified. At remanence the film exhibits a demagnetized labyrinth domain state, consistent with the sheared out-of-plane hysteresis loop in Fig. 1c, inset. With increasing out-of-plane field $B_z > 0$, the up domains (dark contrast) grow while the down domains (light contrast) contract into narrow labyrinth domains, vanishing at saturation.

The domain width reflects the balance between the decreased demagnetizing energy and increased domain wall energy in the multidomain state. The latter scales with the domain wall surface energy density $\sigma_{\text{DW}} = 4\sqrt{AK_{\text{u,eff}}} - \pi|D|$, where A is the exchange stiffness, $K_{\text{u,eff}}$ is the effective uniaxial anisotropy constant, and D is the DMI constant^{25,26}. Hence, σ_{DW} is lowered and domain formation is more favourable whenever D is finite. Measuring the domain spacing therefore provides a convenient means to quantify σ_{DW} , and hence to estimate $|D|$, using well-established analytical models of domain widths in multilayer films²⁷.

The high spatial resolution (~ 25 nm) of MTXM allowed measurement of the domain widths d_{\uparrow} and d_{\downarrow} of up and down domains, respectively, as a function of increasing B_z . At low fields,

¹Department of Materials Science and Engineering, Massachusetts Institute of Technology, Cambridge, Massachusetts 02139, USA. ²Institut für Physik, Johannes Gutenberg-Universität Mainz, 55099 Mainz, Germany. ³Graduate School of Excellence Materials Science in Mainz, Staudinger Weg 9, 55128 Mainz, Germany. ⁴Center for X-ray Optics, Lawrence Berkeley National Laboratory, Berkeley, California 94720, USA. ⁵Daegu Gyeongbuk Institute of Science and Technology, Daegu 711-873, Korea. ⁶Max Planck Institute for Intelligent Systems, 70569 Stuttgart, Germany. ⁷Materials Sciences Division, Lawrence Berkeley National Laboratory, Berkeley, California 94720, USA. ⁸Department of Physics, University of California, Santa Cruz, California 94056, USA. *e-mail: klaeui@uni-mainz.de; gbeach@mit.edu

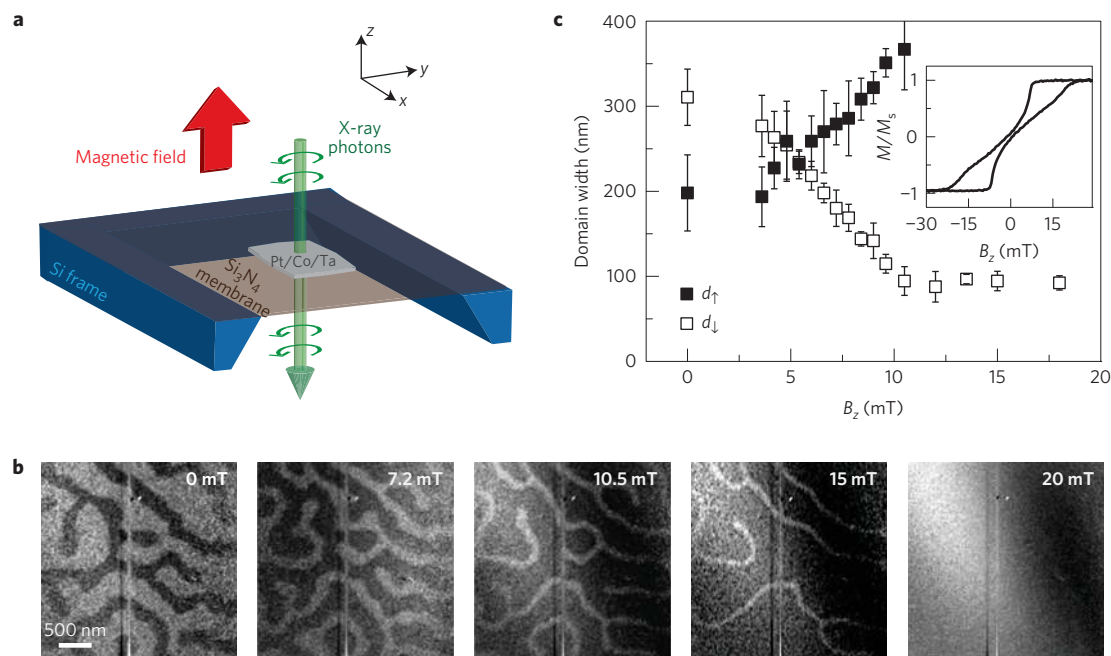


Figure 1 | Soft X-ray imaging of domain structure. **a**, Schematic of MTXM geometry. **b**, Series of MTXM images acquired after negative field saturation for several increasing fields $B_z > 0$ for a continuous Pt/Co/Ta film. Dark and light contrast correspond to magnetization oriented up (along $+z$) and down (along $-z$), respectively. **c**, Width of up and down domains versus B_z , determined from MTXM images. Error bars denote standard deviation of ten individual width measurements. The inset shows a hysteresis loop for a companion film grown on a naturally oxidized Si wafer with magnetization (M) normalized to the saturation magnetization (M_s) versus out-of-plane field B_z .

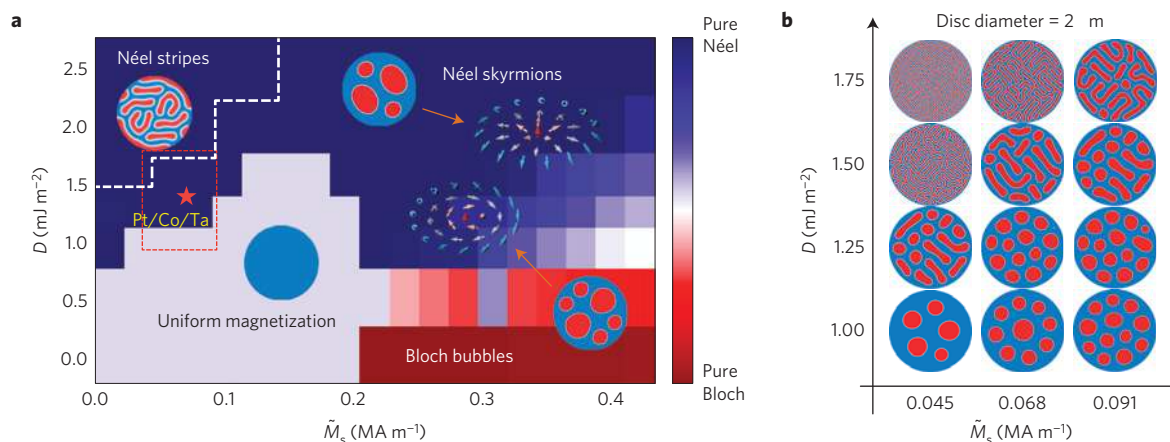


Figure 2 | Spin structure phase diagram. **a**, Representation of the stable ground states for 400 nm discs as a function of saturation magnetization and DMI. The colour scale indicates the domain wall angle evolving from a pure Bloch to a pure Néel configuration with increasing DMI. Insets are exemplary micromagnetically computed domain structures, with red and blue corresponding to up and down magnetization. The red star indicates the material parameters corresponding to the Pt/Co/Ta sample used in experiments. The red dashed box indicates the region corresponding to the simulations shown in panel **b**. **b**, Examples of stable spin structures for 2 μm discs for small variations close to the experimental materials parameters showing that in this regime the ground state is very sensitive to variations in the magnetic parameters.

d_\uparrow and d_\downarrow vary linearly with B_z , maintaining a constant domain period $d = d_\uparrow + d_\downarrow \approx 480$ nm. At higher field d_\uparrow diverges whereas d_\downarrow approaches a terminal width $d_{\downarrow, \text{min}} \approx 100$ nm at $B_z \approx 10$ mT, showing little further variation until saturation. We note that in Fig. 1c, the large apparent remanent magnetization and coercivity (field where up and down domains are the same width) suggested by the low-field MTXM images most likely arise from a large remanent field in the electromagnet, which has not been corrected for.

These behaviours are well described by analytical domain-spacing models for multilayer films²⁷, from which we find $\sigma_{\text{DW}} = 1.3 \pm 0.2 \text{ mJ m}^{-2}$ (see Supplementary Information 2 for details). This is much smaller than $4\sqrt{AK_{\text{u,eff}}} \approx 5.3 \text{ mJ m}^{-2}$ expected

in the absence of DMI, implying a large $|D| = 1.3 \pm 0.2 \text{ mJ m}^{-2}$. Micromagnetic simulations of the domain spacing (see Supplementary Information 2 and Supplementary Fig. 2) corroborated this result. We also examined bubble domain expansion in single-layer films (Supplementary Information 3), which exhibits asymmetry under in-plane field application demonstrating DMI-stabilized Néel domain walls with left-handed chirality, as expected because of the strong interfacial DMI.

Figure 2 summarizes micromagnetic simulations (see Methods) that predict a stable skyrmion lattice in laterally confined geometries for certain combinations of DMI and saturation magnetization \tilde{M}_s . Figure 2a depicts the static magnetic configuration of a

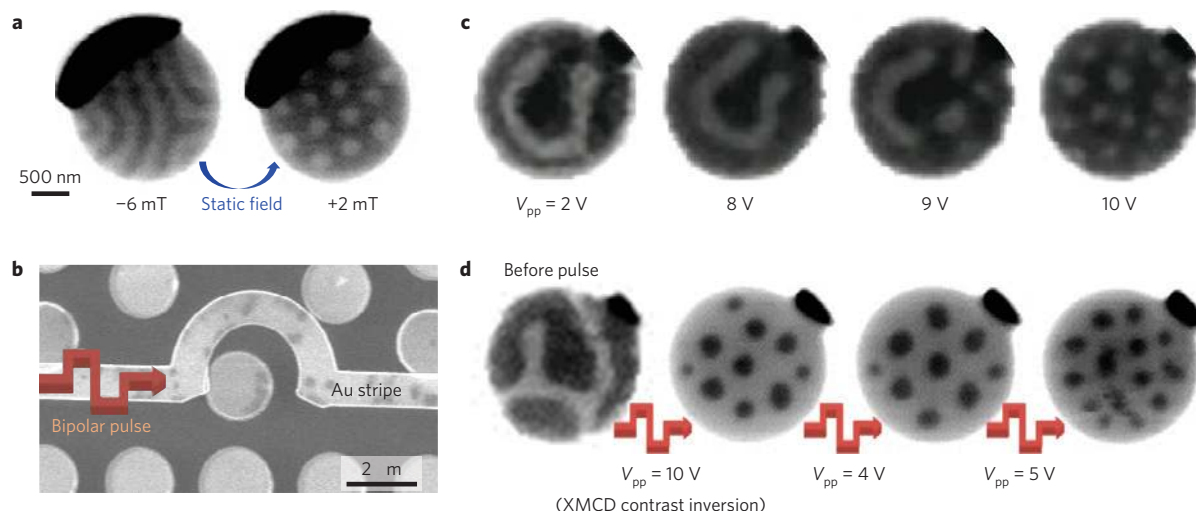


Figure 3 | Skyrmion lattice generation. **a**, STXM images of the domain state in a 2 μm Pt/Co/Ta disc at $B_z = -6$ mT (left) and after subsequently applying $B_z = 2$ mT (right). **b**, Scanning electron micrograph of a magnetic disc array with a Au microcoil patterned around one disc. **c**, Sequence of STXM images after applying bipolar pulse trains (peak-to-peak voltage amplitude V_{pp}) with the microcoil, showing transformation from labyrinth stripe domain into skyrmion lattice. **d**, An initial labyrinth domain state was generated by static field (first image) and then transformed into a hexagonal skyrmion lattice by applying a bipolar pulse train with $V_{pp} = 10$ V (second image). The last two images were acquired after applying $V_{pp} = 4$ V and $V_{pp} = 5$ V, respectively. Dark (light) contrast corresponds to up (down) magnetization in all STXM images except for the last three in **d**, where the X-ray magnetic circular dichroism (XMCD) contrast was inverted.

400-nm-diameter disc as a function of $|D|$ and \tilde{M}_s , which parameterize the DMI and magnetostatic energies that prefer non-uniform ground states. Here, $\tilde{M}_s = M_s t_{\text{Co}} / \Lambda$ is the volume-averaged saturation magnetization, where t_{Co} is the Co layer thickness and Λ is the multilayer period. For large \tilde{M}_s the magnetostatic energy dominates, stabilizing magnetic bubble skyrmions that transition from achiral Bloch to homochiral Néel skyrmions with increasing $|D|$.

For smaller \tilde{M}_s , in the range corresponding to the experimental $\tilde{M}_s = 6.8 \times 10^4 \text{ A m}^{-1}$, the magnetostatic energy alone is insufficient to generate a non-uniform state. For small $|D|$ in this regime, only the uniformly magnetized state can be stabilized, indicating that the experimentally observed multidomain states are driven by the DMI. In the low- \tilde{M}_s regime, as $|D|$ is increased, the uniformly magnetized state gives way to a DMI-stabilized Néel skyrmion lattice phase, and finally to a Néel labyrinth phase when $|D|$ is large.

Figure 2b shows the magnetic texture calculated in the region where $|D|$ and \tilde{M}_s are close to experimental values. Calculations were performed for a larger 2- μm -diameter disc, corresponding to the experimental geometry described below. For larger discs, the skyrmion lattice phase extends to lower $|D|$ because the disc can accommodate larger-diameter skyrmions. The magnetic configuration and skyrmion size depend sensitively on \tilde{M}_s and $|D|$, and for the parameters of our Pt/Co/Ta films, the labyrinth stripe phase and skyrmion phase are predicted to be close in energy, suggesting that the skyrmion lattice phase might be realized experimentally in this system.

We used scanning transmission X-ray microscopy (STXM) to confirm these predictions experimentally. Figure 3a shows STXM images of the domain structure in a 2- μm -diameter Pt/Co/Ta disc during minor loop cycling of B_z . The left panel shows a parallel stripe phase at $B_z = -6$ mT, which transforms into a symmetric hexagonal skyrmion lattice after B_z is swept to +2 mT, favouring up (dark-contrast) domains. This lattice closely resembles the micromagnetically computed structure in Fig. 2b for the experimental \tilde{M}_s and $|D|$, and the quasistatic transformation between the stripe phase and skyrmion lattice demonstrates that both these phases are metastable. Furthermore, our micromagnetic simulations predict that the skyrmion lattice is stable even at zero

field for this material. To demonstrate this, we show in Fig. 3c,d the dynamical transformation of a labyrinth stripe domain phase into a hexagonal skyrmion lattice at $B_z = 0$, by applying short (6 ns) bipolar field pulses with a lithographically patterned microcoil (Fig. 3b). Bipolar pulses were used to excite the domain structure without causing any significant changes of the relative area of 'up' and 'down' domains. The disc was first saturated in the up state, and then $B_z = -2$ mT was applied to nucleate a down labyrinth stripe domain (light contrast in Fig. 3c) before setting B_z back to zero. The process of lattice formation can be seen as bipolar voltage pulse trains with increasing amplitude V_{pp} are injected into the coil (see Supplementary Fig. 6 for corresponding field profile). As V_{pp} is increased from 2 to 9 V, the stripe domain begins to break into discrete skyrmions starting at one end (Fig. 3c) and after $V_{pp} = 10$ V, the domain structure has completely transformed into a geometrically confined skyrmion lattice. As the total domain area in the process does not change, the system is most likely seeking the most energetically stable configuration while maintaining a fixed net magnetization.

The degree of order and the skyrmion size can be manipulated by low-amplitude pulse excitation (Fig. 3d). After initializing the disc with a down labyrinth domain, B_z was set to zero and a pulse train at $V_{pp} = 10$ V was applied to create a stable array of skyrmions. By applying a small-amplitude pulse train $V_{pp} = 4$ V, the skyrmions relax into a highly ordered hexagonal lattice, without changing their size. Increasing slightly the pulsed field amplitude to $V_{pp} = 5$ V (Fig. 3d) decreases the skyrmion size and increases their density. This result demonstrates that multiple skyrmion diameters can be stabilized in confined geometries, leading to multiple lattice periodicities that are commensurate with the confining geometry, as seen also in simulations (see Supplementary Information 5). The skyrmion size can also be controlled with an externally applied out-of-plane field, and skyrmions can be reduced to <50 nm in diameter (see Supplementary Information 5).

Having established that skyrmions can form stable lattices in this material, we next investigate their manipulation by current in a magnetic track. Recent simulations¹³ suggest that skyrmions in ultrathin films can be efficiently driven by vertical spin current injection, which can occur when charge current flows in an adjacent

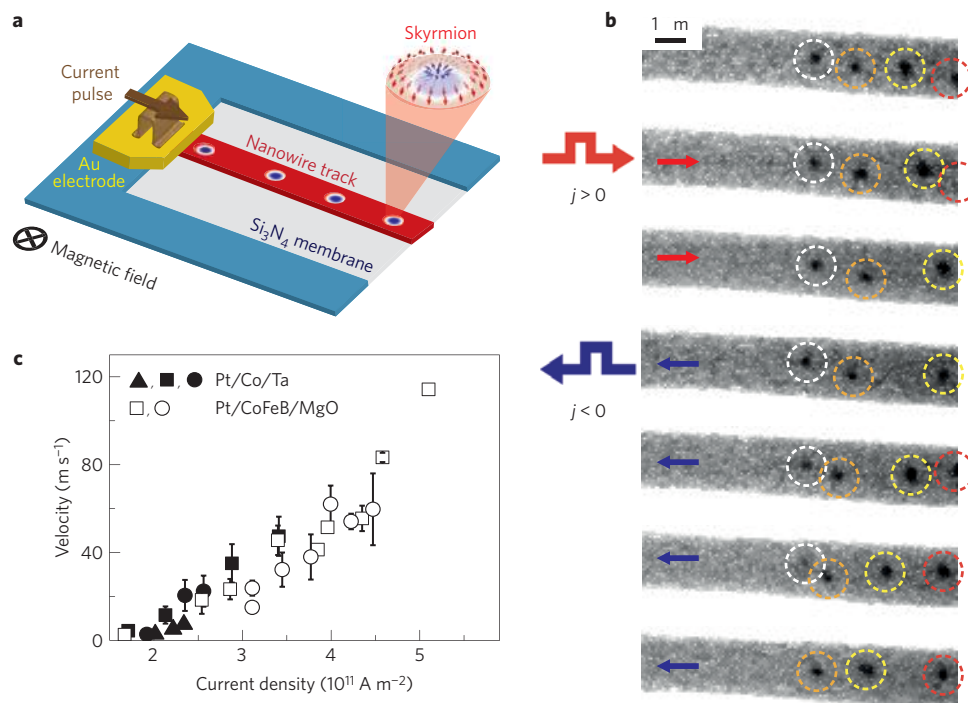


Figure 4 | Current-driven skyrmion motion. **a**, Schematic of a magnetic track on an Si₃N₄ membrane with current contacts and skyrmions stabilized by a down-directed applied magnetic field. **b**, Sequential STXM images showing skyrmion displacement in Pt/Co/Ta after injecting 20 unipolar current pulses along the track, with an amplitude $j_a = 2.2 \times 10^{11} \text{ A m}^{-2}$ and polarity as indicated. Individual skyrmions are outlined in coloured circles for clarity. **c**, Average skyrmion velocity of Pt/Co/Ta (filled symbols) and Pt/CoFeB/MgO (open symbols) versus current density. Different shaped symbols correspond to different devices. Error bars denote standard deviation of multiple measurements.

heavy metal because of the spin Hall effect. In this case, the current exerts a Slonczewski-like torque that can be much stronger than spin-transfer torques from in-plane spin current. As Pt and Ta have large spin Hall angles with opposite signs, the spin Hall currents generated at each interface in Pt/Co/Ta work in concert to generate a large Slonczewski-like torque²⁸. As the spin Hall effect direction of motion of a skyrmion depends on its topology¹³, observations of current-induced displacement can serve to unambiguously verify the topology and chirality of the skyrmions in this system.

In Fig. 4, an external magnetic field B_z was applied to a 2- μm -wide Pt/Co/Ta magnetic track to shrink the zero-field labyrinth domains into a few isolated skyrmions. The track was contacted by Au electrodes at either end for current injection (Fig. 4a). Figure 4b shows a sequence of STXM images of a train of four skyrmions stabilized by B_z . Each image was acquired after injecting 20 current pulses with current-density amplitude $j_a = 2.2 \times 10^{11} \text{ A m}^{-2}$ and duration 20 ns, with the polarity indicated in the figure. Three of the four skyrmions move freely along the track, and can be displaced forward and backward by current, whereas the left-most skyrmion remains immobile, evidently pinned by a defect.

The propagation direction is along the current-flow direction (against electron flow), and this same directionality was observed for skyrmions with oppositely oriented cores. This behaviour is analogous to spin Hall current-driven motion of homochiral Néel domain walls stabilized by interfacial DMI in Pt/Co(Fe)/oxide thin films^{19,20,24}. Micromagnetic simulations (see Supplementary Information 6.1 and Supplementary Fig. 5 for details) show that as is the case for domain walls, spin-Hall-driven displacement along the current-flow direction occurs only for left-handed Néel skyrmions, confirming the topology of the skyrmions in this material.

The average skyrmion velocity was measured versus current density in three different devices, shown in Fig. 4c. We observe a critical current density $j_c \sim 2.0 \times 10^{11} \text{ A m}^{-2}$, below which no

skyrmion motion is observed. Slightly above j_c the skyrmions move at different average speeds in different regions of the track, suggesting a significant influence of local disorder on the dynamics. Interestingly, pinned skyrmions can be annihilated, as seen in the last image of Fig. 4b, where only three skyrmions remain, and the left-most skyrmion becomes pinned at the same location as was the annihilated skyrmion. At higher current densities we observe fast skyrmion motion with velocities approaching 50 m s^{-1} at $j \sim 3.5 \times 10^{11} \text{ A m}^{-2}$.

The experimentally observed critical current density, and the skyrmion velocities that are lower than those calculated for a defect-free sample (see Supplementary Fig. 8) are in sharp contrast to recent micromagnetic studies that predict high skyrmion mobility even in the presence of discrete defects^{10–13}. In those studies, discrete defects were introduced sparsely at a length scale larger than the skyrmion size, so that skyrmions could propagate around them and avoid becoming pinned. In ultrathin films, both the anisotropy and DMI arise from interface coordination, and atomic-scale interface disorder will result in an energy landscape that is inhomogeneous on length scales comparable to and smaller than the skyrmion size. Our micromagnetic simulations (see Supplementary Information 6.2 and 6.3 and Supplementary Figs 9–11 for details) show that short-length-scale dispersion in the local DMI can strongly pin skyrmions, leading to a finite critical current, reduced velocities, and current-induced annihilation of pinned skyrmions, in agreement with our experiments.

These results suggest that more reliable current-driven motion might be achieved by using lower pinning materials. To test this experimentally, we developed [Pt(3 nm)/CoFeB(0.7 nm)/MgO(1 nm)]₁₅ multilayer stacks. Here, amorphous CoFeB was chosen because the absence of grain boundaries leads to lower pinning as compared with polycrystalline Co (see Supplementary Information 3 and Supplementary Fig. 4). The average skyrmion velocity for Pt/CoFeB/MgO versus current

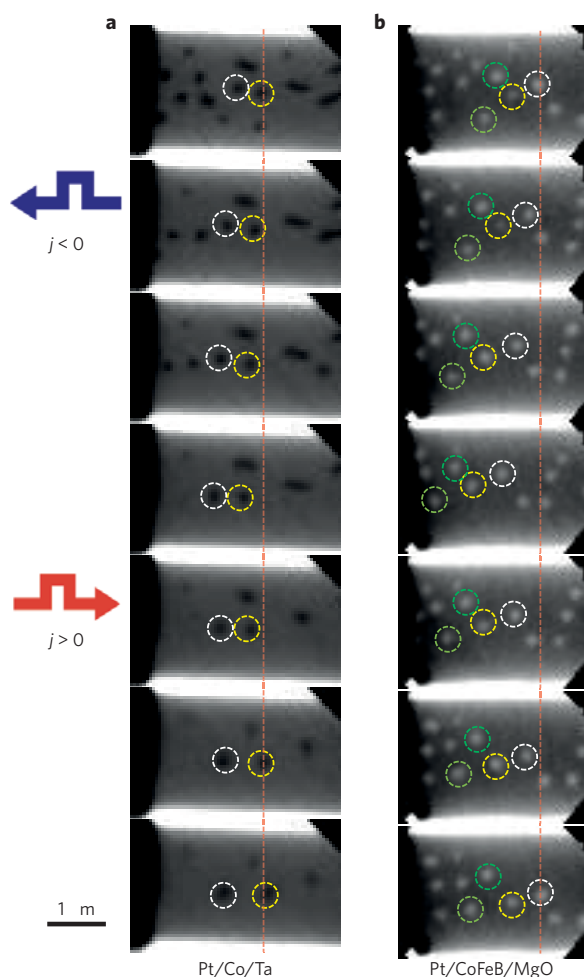


Figure 5 | Skyrmion displacement at high current densities for Pt/Co/Ta and Pt/CoFeB/MgO. a, b, Series of sequential STXM images of skyrmions in Pt/Co/Ta (**a**) and Pt/CoFeB/MgO (**b**) tracks after injecting a series of 5 ns current pulses in the direction shown. The current pulse amplitude was $j_a = 4.8 \times 10^{11} \text{ A m}^{-2}$ for Pt/Co/Ta and $j_a = 3.5 \times 10^{11} \text{ A m}^{-2}$ for Pt/CoFeB/MgO. Several mobile skyrmions are circled for clarity, and vertical dashed lines are included as visual guides.

is shown in Fig. 4b. We observe skyrmion motion in excess of 100 m s^{-1} , and a j_c similar to that in Pt/Co/Ta, despite the smaller torque per unit current density in Pt/CoFeB/MgO (with an effective spin Hall angle ~ 0.07 , compared with ~ 0.34 for Pt/Co/Ta (ref. 28)).

The sequences of images in Fig. 5 compare current-driven skyrmion motion in Pt/Co/Ta (Fig. 5a) and Pt/CoFeB/MgO (Fig. 5b) in the higher velocity regime, highlighting the influence of pinning on the dynamics. In the case of Pt/Co/Ta, skyrmions in some regions of the track move freely at a velocity of $\sim 30 \text{ m s}^{-1}$, whereas others remain pinned and many skyrmions are annihilated by the injected current pulses. Such current-induced annihilation of pinned skyrmions is reproduced in our micromagnetic simulations (see Supplementary Information 6.3).

The corresponding sequence of images for Pt/CoFeB/MgO in Fig. 5b shows skyrmions shifted first leftward and then rightward by current at an average velocity of $\sim 46 \text{ m s}^{-1}$. Here, virtually all of the skyrmions move freely, always against the electron flow direction, and all but one of the initial skyrmions remain after the sequence of current pulses. These results demonstrate for the first time that thin-film metallic ferromagnets can be tailored to allow skyrmions to be displaced robustly at very high velocities, as necessary for devices. We note that here we observe skyrmions in the flow regime, whereas

current-induced skyrmion bubble motion in the creep regime has been recently observed in a different material in ref. 29.

Our results show that in common sputter-deposited transition metal ferromagnets magnetic skyrmions and skyrmion lattices can be stabilized and manipulated at high speeds in confined geometries at room temperature. As the magnetic properties of thin-film heterostructures can be tuned over a wide range by varying layer thicknesses, composition and interface materials, this work highlights the possibility to engineer the properties of skyrmions and their dynamics using materials that can be readily integrated into spintronic devices.

Methods

Methods and any associated references are available in the [online version of the paper](#).

Received 22 June 2015; accepted 29 January 2016;
published online 29 February 2016

References

- Rößler, U. K., Bogdanov, A. N. & Pfleiderer, C. Spontaneous skyrmion ground states in magnetic metals. *Nature* **442**, 797–801 (2006).
- Mühlbauer, S. *et al.* Skyrmion lattice in a chiral magnet. *Science* **323**, 915–919 (2009).
- Münzer, W. *et al.* Skyrmion lattice in the doped semiconductor $\text{Fe}_{1-x}\text{Co}_x\text{Si}$. *Phys. Rev. B* **81**, 041203 (2010).
- Yu, X. Z. *et al.* Real-space observation of a two-dimensional skyrmion crystal. *Nature* **465**, 901–904 (2010).
- Yu, X. Z. *et al.* Near room-temperature formation of a skyrmion crystal in thin-films of the helimagnet FeGe. *Nature Mater.* **10**, 106–109 (2011).
- Heinze, S. *et al.* Spontaneous atomic-scale magnetic skyrmion lattice in two dimensions. *Nature Phys.* **7**, 713–718 (2011).
- Jonietz, F. *et al.* Spin transfer torques in MnSi at ultralow current densities. *Science* **330**, 1648–1651 (2010).
- Schulz, T. *et al.* Emergent electrodynamics of skyrmions in a chiral magnet. *Nature Phys.* **8**, 301–304 (2012).
- Yu, X. Z. *et al.* Skyrmion flow near room temperature in an ultralow current density. *Nature Commun.* **3**, 988 (2012).
- Iwasaki, J., Mochizuki, M. & Nagaosa, N. Universal current-velocity relation of skyrmion motion in chiral magnets. *Nature Commun.* **4**, 1463 (2013).
- Fert, A., Cros, V. & Sampaio, J. Skyrmions on the track. *Nature Nanotech.* **8**, 152–156 (2013).
- Iwasaki, J., Mochizuki, M. & Nagaosa, N. Current-induced skyrmion dynamics in constricted geometries. *Nature Nanotech.* **8**, 742–747 (2013).
- Sampaio, J., Cros, V., Rohart, S., Thiaville, A. & Fert, A. Nucleation, stability and current-induced motion of isolated magnetic skyrmions in nanostructures. *Nature Nanotech.* **8**, 839–844 (2013).
- Dzyaloshinsky, I. A thermodynamic theory of ‘weak’ ferromagnetism of antiferromagnetics. *J. Phys. Chem. Solids* **4**, 241–255 (1958).
- Moriya, T. Anisotropic superexchange interaction and weak ferromagnetism. *Phys. Rev.* **120**, 91–98 (1960).
- Uchida, M., Onose, Y., Matsui, Y. & Tokura, Y. Real-space observation of helical spin order. *Science* **311**, 359–361 (2006).
- Bode, M. *et al.* Chiral magnetic order at surfaces driven by inversion asymmetry. *Nature* **447**, 190–193 (2007).
- Fert, A. & Levy, P. M. Role of anisotropic exchange interactions in determining the properties of spin-glasses. *Phys. Rev. Lett.* **44**, 1538–1541 (1980).
- Emori, S., Bauer, U., Ahn, S.-M., Martinez, E. & Beach, G. S. D. Current-driven dynamics of chiral ferromagnetic domain walls. *Nature Mater.* **12**, 611–616 (2013).
- Ryu, K.-S., Thomas, L., Yang, S.-H. & Parkin, S. Chiral spin torque at magnetic domain walls. *Nature Nanotech.* **8**, 527–533 (2013).
- Pizzini, S. *et al.* Chirality-induced asymmetric magnetic nucleation in Pt/Co/AlO_x ultrathin microstructures. *Phys. Rev. Lett.* **113**, 047203 (2014).
- Emori, S. *et al.* Spin Hall torque magnetometry of Dzyaloshinskii domain walls. *Phys. Rev. B* **90**, 184427 (2014).
- Torreson, J. *et al.* Interface control of the magnetic chirality in CoFeB/MgO heterostructures with heavy-metal underlayers. *Nature Commun.* **5**, 4655 (2014).
- Lo Conte, R. *et al.* Role of B diffusion in the interfacial Dzyaloshinskii–Moriya interaction in Ta/Co₂₀Fe₆₀B₂₀/MgO nanowires. *Phys. Rev. B* **91**, 014433 (2015).
- Heide, M., Bihlmayer, G. & Blügel, S. Dzyaloshinskii–Moriya interaction accounting for the orientation of magnetic domains in ultrathin films: Fe/W(110). *Phys. Rev. B* **78**, 140403 (2008).

26. Thiaville, A., Rohart, S., Jué, É., Cros, V. & Fert, A. Dynamics of Dzyaloshinskii domain walls in ultrathin magnetic films. *Europhys. Lett.* **100**, 57002 (2012).
27. Malek, Z. & Kambersky, V. On the theory of the domain structure of thin films of magnetically uniaxial materials. *Czech. J. Phys.* **8**, 416–421 (1958).
28. Woo, S., Mann, M., Tan, A. J., Caretta, L. & Beach, G. S. D. Enhanced spin-orbit torques in Pt/Co/Ta heterostructures. *Appl. Phys. Lett.* **105**, 212404 (2014).
29. Jiang, W. *et al.* Blowing magnetic skyrmion bubbles. *Science* **349**, 283–286 (2015).

Acknowledgements

Work at MIT was primarily supported by the US Department of Energy (DOE), Office of Science, Basic Energy Sciences (BES) under Award No. DE-SC0012371 (sample fabrication and MTXM and STXM experiments). The operation of the X-ray microscope at the Advanced Light Source was supported by the Director, Office of Science, Office of Basic Energy Sciences, Scientific User Facilities Division, of the US Department of Energy under Contract No. DE-AC02-05-CH11231. M.-Y.I. acknowledges support from the Leading Foreign Research Institute Recruitment Program (Grant No. 2012K1A4A3053565) through the National Research Foundation of Korea (NRF) funded by the Ministry of Education, Science and Technology (MEST). P.F. acknowledges support from the Director, Office of Science, Office of Basic Energy Sciences, Materials Sciences and Engineering Division, of the US Department of Energy under Contract No. DE-AC02-05-CH11231 within the Non-Equilibrium Magnetic Materials programme. G.S.D.B. acknowledges support from C-SPIN, one of the six SRC STARnet Centers, sponsored by MARCO and DARPA. M.K. and the group at Mainz acknowledge support by the DFG, the Graduate School of Excellence Materials Science in Mainz (MAINZ, GSC 266), the EU (MASPIC, ERC-2007-StG 208162; WALL, FP7-PEOPLE-2013-ITN 608031; MAGWIRE, FP7-ICT-2009-5), the MOGON (ZDV Mainz computing centre) and the Research Center of Innovative and Emerging Materials

at Johannes Gutenberg University (CINEMA). B.K. is grateful for financial support by the Carl-Zeiss-Foundation. K.L. gratefully acknowledges financial support by the Graduate School of Excellence Materials Science in Mainz (MAINZ). S.W. acknowledges support from the Kwanjeong Foundation. L.C. acknowledges support by the NSF Graduate Research Fellowship Program. Measurements were carried out at the MAXYMUS endstation at Helmholtz-Zentrum Berlin. We thank HZB for the allocation of beamtime.

Author contributions

S.W., P.F., M.K. and G.S.D.B. designed and initiated the research. S.W. and I.L. fabricated devices and S.W., I.L., L.C. and P.A. performed the film characterization. L.C. performed MOKE measurements of bubble domain expansion. S.W., M.-Y.I., L.C., M.M., K.L., I.L. and P.F. performed X-ray imaging experiments using MTXM at the Advanced Light Source in Berkeley, California. S.W., K.L., L.C., K.R., A.K., R.M.R. and M.W. conducted STXM experiments at the MAXYMUS beamline at the BESSY II synchrotron in Berlin. K.L., B.K. and M.K. performed and analysed the micromagnetic simulations. M.-A.M. provided technical input on sample design. B.K. derived the effective medium scaling laws and wrote the corresponding section in the Supplementary Information. P.A. and I.L. performed the analytical analysis of domain-spacing data. All authors participated in the discussion and interpreted results. S.W. drafted the manuscript and G.S.D.B. revised it with assistance from P.F. and M.K. All authors commented on the manuscript.

Additional information

Supplementary information is available in the [online version of the paper](#). Reprints and permissions information is available online at www.nature.com/reprints. Correspondence and requests for materials should be addressed to M.K. or G.S.D.B.

Competing financial interests

The authors declare no competing financial interests.

Methods

The [Pt(3 nm)/Co(0.9 nm)/Ta(4 nm)]₁₅ and [Pt(4.5 nm)/CoFeB(0.7 nm)/MgO(1.4 nm)]₁₅ films were grown by d.c. magnetron sputtering at room temperature under 3 mtorr Ar at a background pressure of $\sim 2 \times 10^{-7}$ torr. A thin (3 nm) Ta seed layer was deposited before growing the multilayer stacks. Fifteen layer repetitions were grown to enhance magnetic contrast in the X-ray magnetic circular dichroism (XMCD) signal and to more readily destabilize the uniformly magnetized state on account of the increased demagnetizing field. Samples were grown on 100-nm-thick Si₃N₄ membranes for XMCD imaging in transmission geometry. Nominally identical companion films were grown on thermally oxidized Si wafers for magnetic characterization by vibrating sample magnetometry (VSM). VSM measurements for Pt/Co/Ta yield an in-plane saturation field $\mu_0 H_k = 0.5$ T, and a saturation magnetization $M_s = 6 \times 10^5$ A m⁻¹, normalized to the nominal Co volume. This corresponds to a volume-averaged magnetization $\bar{M}_s = 6.8 \times 10^4$ A m⁻¹ (averaged over the total film volume). VSM measurements for Pt/CoFeB/MgO yield field $\mu_0 H_k = 0.7$ T and $M_s = 4.3 \times 10^5$ A m⁻¹, normalized to the nominal CoFeB volume.

The disc and track structures in Figs 3–5 were patterned using electron beam lithography and lift-off. The microcoil in Fig. 3 and current injection contacts in Figs 4 and 5 were sputtered Ti(5 nm)/Au(100 nm) bilayers patterned using a second lithography step.

Samples for XMCD imaging were oriented with the surface normal parallel to the circularly polarized X-ray beam (Fig. 1a), so that the XMCD contrast is sensitive to the out-of-plane magnetization component. The images in Fig. 1 of the main text were acquired using full-field magnetic transmission soft X-ray microscopy (MTXM) performed at the XM-1 beamline 6.1.2 at the Advanced Light Source. The images in Figs 3–5 of the main text were acquired using scanning transmission X-ray microscopy (STXM) at the MAXYMUS beamline at the BESSY II synchrotron.

The bipolar field pulses applied using the microcoil in Fig. 3 of the main text were generated by injecting square bipolar voltage pulses with peak-to-peak amplitude V_{pp} , and a length of 6 ns. The pulse trains referred to in the main text consisted of 30 s applications of these bipolar pulses at a repetition rate of 1.43 MHz. A peak-to-peak voltage amplitude $V_{pp} = 1$ V corresponds to a maximum current amplitude of 6 mA, or a current density of 6×10^{10} A m⁻². Details of the coil geometry and calculated magnetic field profile are discussed in Supplementary Information 3.

Current-driven skyrmion motion experiments were performed using STXM and full-field MTXM. The magnetic tracks corresponding to Pt/Co/Ta Device 1 in Fig. 4, measured by STXM, were 300 μ m long, which limited the maximum

current density to $\sim 2.3 \times 10^{11}$ A m⁻² because of the resistance of the track and the limited voltage available from the voltage pulser. Pt/Co/Ta Devices 2 and 3 in Fig. 4 were measured using MTXM, and were 100 μ m long, so that larger current densities could be used owing to the smaller device resistance. In this case, current densities above $\sim 4 \times 10^{11}$ A m⁻² led to damage of the membranes, which limited the maximum current applied in Fig. 4c. The Pt/Co/Ta and Pt/CoFeB/MgO devices in Fig. 5 and the Pt/CoFeB/MgO devices used for Fig. 4c were 2 μ m wide and 5 μ m long. Skyrmion velocities were determined by injecting a low-duty-cycle train of current pulses, and computing an average velocity using the total displacement and integrated pulse time. Six to twelve such displacements were recorded, and the mean and standard deviations of the individual velocity measurements are reported in Fig. 4c. Current densities were obtained by averaging the injected current across the Pt and Co or CoFeB layers, because the Ta and MgO layers have a much higher resistivity and therefore do not shunt a significant fraction of the current. The resistance of the 15-layer Pt/CoFeB/MgO stack is ~ 15 times lower than a single-layer Pt/CoFeB/MgO track, indicating uniform current flow across the 15 repeats.

Micromagnetic simulations were performed using the MicroMagnum micromagnetics software, available at <http://micromagnum.informatik.uni-hamburg.de>. For the micromagnetic simulations, we used an effective medium approach to model the multilayer film as a single uniform layer³⁰, described in detail in Supplementary Information 1, and thus to reduce the necessary computational resources. The systems were modelled with mesh sizes of 2×2 nm² and 4×4 nm² for the 400-nm- or 2,000-nm-diameter discs, respectively. To check for consistency, some geometries were modelled with mesh sizes down to 1×1 nm² and no difference was found. The simulations used a saturation magnetization 6×10^5 A m⁻¹, an exchange constant $A = 1.0 \times 10^{-11}$ J m⁻¹, and an out-of-plane uniaxial anisotropy with in-plane saturation field $\mu_0 H_k = 0.5$ T, corresponding to the values measured by VSM. For simulations of current-driven skyrmion dynamics, a spin Hall angle $\theta_{\text{SHE}} = +0.35$ was used, corresponding to the value for Pt/Co/Ta films reported in ref. 28. The implementation of the current-induced torque due to the spin Hall effect is described in Supplementary Information 1. The simulations of the magnetization patterns in the discs in Fig. 2a of the main text were obtained by relaxing from an initial state corresponding to a 4×4 checkerboard pattern.

References

30. Honda, S., Ikegawa, Y. & Kusuda, T. Magnetostatic energy and magnetization process in multilayers with perpendicular anisotropy. *J. Magn. Magn. Mater.* **111**, 273–292 (1992).